# A 107 pJ/b TX 260 pJ/b RX Ultra-Low-Power MEMS-based Transceiver with Wake-up in ISM-bands for IoT Applications

Kai Tang, *Member, IEEE,* Chuanshi Yang, Yanshu Guo, *Member, IEEE,* Nan Wang, Yao Zhu, *Member, IEEE,* Ying Zhang, Eldwin Jiaqiang Ng, Joshua En-Yuan Lee, Zhongyuan Fang, *Member, IEEE,* Wensong Wang, *Senior Member, IEEE,* Hanjun Jiang, *Senior Member, IEEE,* Chun-Huat Heng, *Senior Member, IEEE,* Yuanjin Zheng, *Senior Member, IEEE*

***Abstract*— This paper presents an ultra-low-power MEMS-based phase-tracking FSK TRX with an embedded envelop detector based OOK WuRX. The system supports a shared antenna interface of FSK-matched filter for TRX and a matching network for the FSK RX and OOK WuRX. To consume less power, the transmitter employs an adaptive fast switching technique for FSK/OOK modulator, and uses a high-Q MEMS resonator to get frequency stability. In addition, for better interference filtering, the MEMS-based modulator is shared to provide LO in FSK RX as it owns inherent side-lobe suppression. To support higher blocker/interference rejection with relatively low power, MEMS-based FSK-matched filter plus matching network with current-reuse LNA are co-designed to provide additional passive gain. Fabricated in 65-nm CMOS process, the TX generates FSK signals of -11.2 dBm output power at ISM-915 MHz and the data rate is up to 6Mb/s. At 1 MHz offset, the measured phase noise is -140.2 dBc/Hz and -139.3 dBc/Hz at 926.3 MHz and 932.4 MHz, respectively. By sharing the modulator, the RX exhibits -36.2 dB in-band SIR, -77.5 dBm sensitivity at BER of $10^{-3}$ working under 2 Mb/s data rate. The TX, FSK RX and WuRX consume 642 µW@6 Mb/s, 520 µW@2 Mb/s and 86 µW@200 kb/s, leading to the energy efficiency of 107 pJ/b, 260 pJ/b and 430 pJ/b, respectively. The proposed TX achieves over 1.5× better energy efficiency than state-of-art results and the FSK RX attains among the best FoM with the sensitivity of -77.5 dBm, which are well suited for energy-efficient pico-IoT applications.**

***Index Terms*— ULP, MEMS, CMOS integrated circuit, FSK, OOK, wake-up, transceiver, ISM, IoT.**

## I. Introduction

MAXIMIZING the energy efficiency while maintaining performance is paramount in radio transceiver design for ultra-low-power (ULP) IoT applications. IoT transceiver (TRX) deployments are envisioned to have low power, low data-rate (~kb/s) wake-up receiver (WuRX) and Mb/s primary receive/transmitter (RX/TX) modes for long battery lifetimes, also where they envision massive numbers of interconnected sensors; however, the cost of replacing/recharging batteries can become an impediment to their large deployment. To enable efficient IoT applications, a single-chip wireless transceivers (TRXs) need to operate with high-performance under low power consumption. Moreover, the TRXs are required to support multi-band operation, especially for transceivers applied targeting ultra-low-power (ULP) application scenarios [1-12]. This is particularly true for many IoT applications deployed for wireless sensor networks (WSN) or wireless body area networks (WBAN), where the devices are mainly powered by small-sized batteries with limited power capacity. Therefore, many energy-efficient wireless receivers or transmitters were reported to achieve both high data rate and small form factors [1, 4-6]. In addition to on–off keying (OOK) modulation, constant-envelope frequency shift keying (FSK) modulation is commonly leveraged for low-power transceiver design because of its better interferer resilience [1, 3, 5]. Open loop direct modulation transmitter has demonstrated its power advantage due to its architectural simplicity. However, the sensitivity is significantly deteriorated by the poor phase noise (PN) and large frequency drift of free-running oscillator. Injection-lock or PLL-based architecture employs external bulky crystal oscillators to reduce the PN and frequency drift, at the expense of size constraint and settling time. To improve the performance of direct FSK modulation TXs or RXs, the high-Q MEMS,

Manuscript received on 23 March, 2022. This work was supported by the A*STAR SERC AME program Nano-systems at the edge: A18A4b0055. K. (Corresponding authors: Yuanjin Zheng, Chun-Huat Heng and Hanjun Jiang.)

K. Tang is with Nanyang Technological University, Singapore (ktang@ntu.edu.sg), now at College of Electrical and Information Engineering, Hunan University, China (ktang@hnu.edu.cn).

C. Yang, Y. Guo, Z. Fang, W. Wang and Y. Zheng are with the School of Electrical and Electronic Engineering, Nanyang Technological University, Singapore 639798. (yjzheng@ntu.edu.sg, E150204@e.ntu.edu.sg.).

N. Wang, Y. Zhu, Y. Zhang, E. Ng, J. E.-Y. Lee are with A*STAR (Agency for Science, Technology and Research), Institute of Microelectronics, Singapore.

H. Jiang is with the School of Integrated Circuits, Tsinghua University, Beijing 10084, China. (jianghanjun@tsinghua.edu.cn)

C.-H. Heng is with National University of Singapore, Singapore. (elehch@nus.edu.sg)

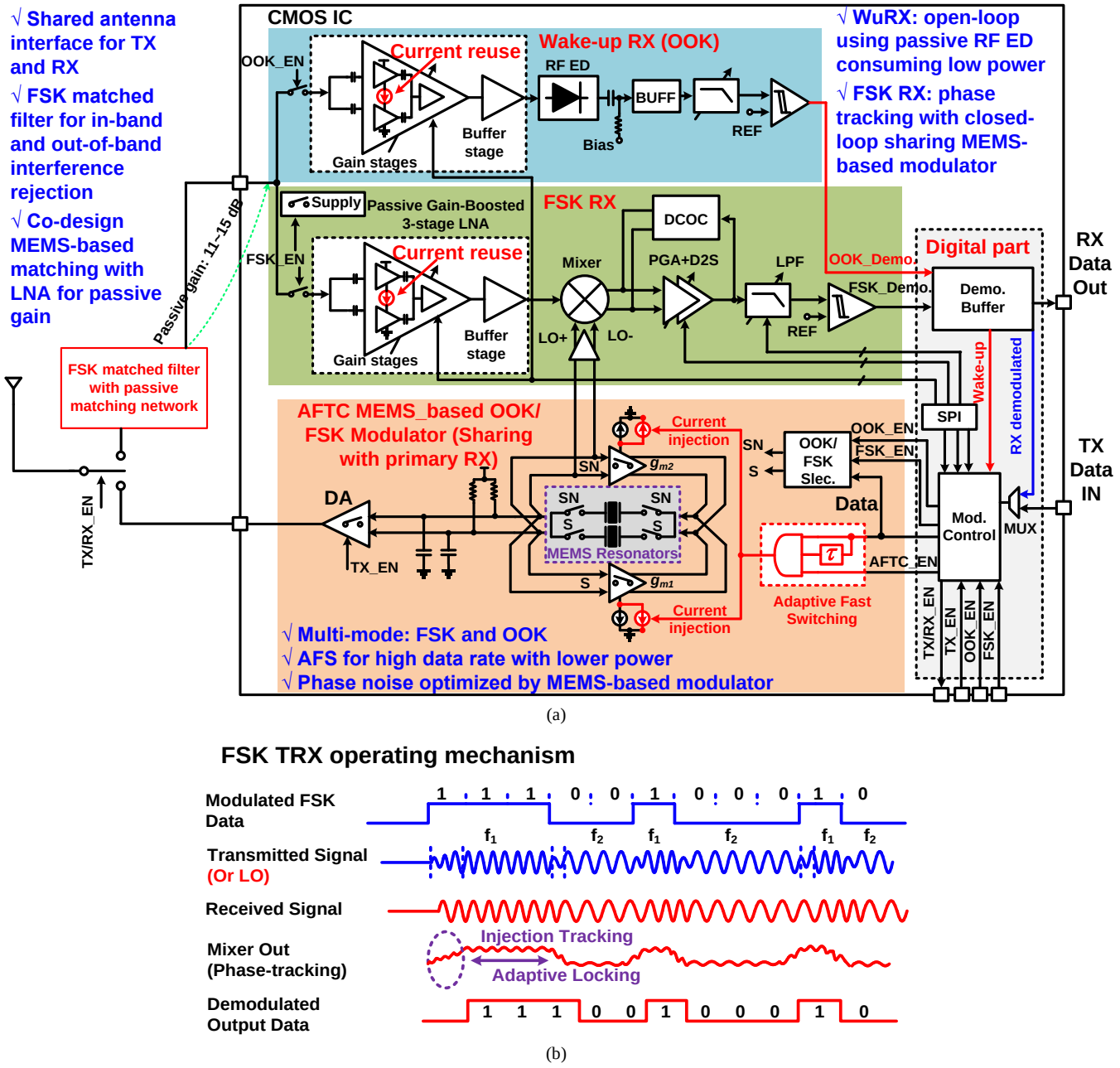


(a)




(b)

Fig. 1. (a) The proposed system architecture of MEMS-based phase-tracking OOK/FSK transceiver with wake-up path and (b) FSK TRX system operating mechanism.

surface acoustic wave (SAW), or bulk acoustic wave (BAW) resonator can be employed, which would achieve better phase noise performance as well as less power dissipation [2, 8, 13]. Several radios had utilized amplitude modulation or envelope detection (ED) to remove the demand of precise frequency references to save power, achieving energy efficiency of 610 pJ/b [1-2]. But these implementations suffer from poor frequency selectivity and sensitivity. Energy-efficient phase-domain RXs have gained interest recently [3-4]. In [3], a zero-IF digitally-controlled-oscillator (DCO) based phase-tracking RX achieved an energy efficiency of 770 pJ/b at 2 Mb/s. Nevertheless, the sensitivity is degraded since a poor deviation frequency control, and an undefined initial carrier frequency may track to interference by risk. In [4], it utilized a hybrid loop filter for better interference filtering to attain good sensitivity and selectivity, and an ADPLL to define the initial frequency. This increases the architecture's complexity and trades-off the energy efficiency. Also, the antenna should be shared for the transmitter and receivers (primary RX or WuRX) in the ULP TRX which may make the challenging to share the high-Q WuRX matching network with the primary radio [5-6].

The article presents a completed ULP MEMS-based TRX for IoT applications which compose of a MEMS-based TX, a phase-tracking FSK RX with embedded ED OOK WuRX, illustrated in Fig. 1. Compared to other state-of-arts, the advantage of the implementation lies in three aspects. (1) To consume less power, the transmitter employs an adaptive fast switching (AFS) technique for FSK/OOK modulation, and uses

a high-Q dual MEMS resonator to get better frequency stability. (2) By reusing the dual MEMS-based oscillator within a phase-tracking RX, it attains better interference filtering due to inherent side-lobe suppression of the MEMS oscillator. This leads to better sensitivity and selectivity without the need of hybrid filtering in [4]. (3) MEMS-based FSK matched filter plus matching network with current-reuse LNA is co-designed to provide additional passive gain, and better both in-band and out-of-band blocker/ interference rejection while consuming low power. The consideration and implementation of system architecture, circuit designs, and experimental results are presented in detail. The rest of the paper is organized as follows. The analysis and system level design considerations of the proposed TRX are elaborated in Section II; in Section III and Section IV, the design details and some measured results of the building block circuits of TX and RX are described, respectively; Section V presents the fabricated TRX and the measured performance of it. Finally, Section VI concludes the article.

## II. System Level Considerations

For ULP applications, the size of the sensor nodes is aimed at as small as a coin size or several $cm^2$ while it is working with wake-up radios and MEMS-based energy harvesting which could cover a 10-m range with the data-packet size of <100k bytes [5]. The sensor nodes could be used in different applications such as factory automation, IoT, smart city. To make the nodes smaller, operating frequencies of higher than hundreds of MHz, e.g., in the 433, 867, 915, or 2400-MHz ISM bands, are always be used, which could make the antenna size more compact with decent gain to relax the required parameters for the TRX.

### A. MEMS-based transceiver architecture

Fig. 1 draws the system diagram and operation mechanism of the proposed TRX, illustrating a direct FSK/OOK TX, a zero-IF phase-tracking FSK RX and OOK WuRX. The FSK TRX operates in half-duplex mode, which allows the TX and RX to reuse the MEMS-based binary FSK/OOK modulator. This modulator employs high-Q (~1000) dual MEMS resonators which are switched by the input modulated data to obtain dual frequency output with a modulation index of 0.13~0.25 (FSK), possible centered at ISM-915 MHz band, ISM-867 MHz band or ISM-433 MHz band. The AFS technique is proposed to support high data rate. During TX operation, the FSK/OOK generator is directly modulated with input binary data, and its output is subsequently connected to a driving amplifier (DA) to drive the antenna. During the RX operation, the modulator working as FSK mode is reused as the binary oscillator. To further improve the RX sensitivity and interference rejection, a current-reuse LNA is co-designed with a FSK matched filter through matching network, which will provide additional passive gain and high-Q filtering for the received signal. Combined with a single-balanced mixer, a programmable gain amplifier (PGA) with DC offset cancel (DCOC) loop, a tunable low-pass filter (LPF), a comparator and the FSK modulator, a zero-IF phase-tracking RX is formed, which can achieve >40 dB dynamic range and >30 dB in-band/>40 dB out-of-band interference suppression. A feedforward frequency mismatch cancellation path is also implemented and used as a reference input to the comparator. By reusing the LNA, LPF and comparator, a RF ED-based OOK WuRX path is implemented as a low rate wake up receiver (<200 kbps) when working at event driven burst mode.

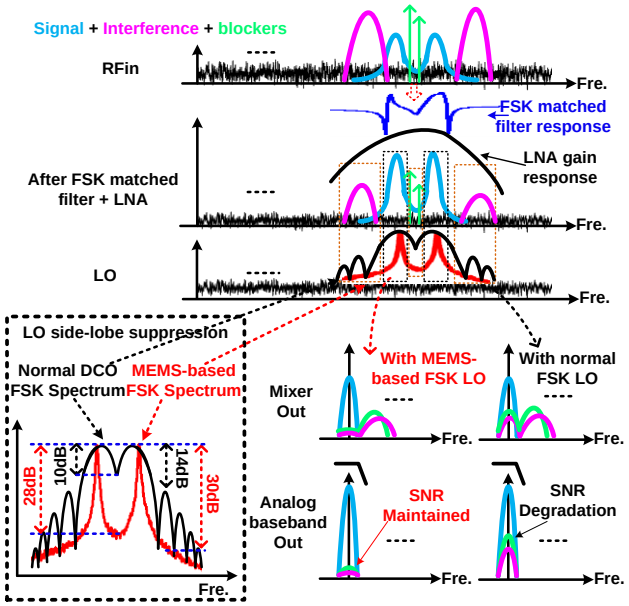


Fig. 2. Illustration of the phase-domain RX with interference resilience by MEMS-based LO.

### B. FSK interference/blocker rejection and coherent detection

As discussed in [7], it is crucial to achieve both good sensitivity and frequency selectivity which is needed to tradeoff between the loop delay and interference filtering in a typical phase-tracking RX. Issue the $t_{loop}$ is the total loop delay of the phase-tracking loop as the RX loop delay and it is mainly contributed by the baseband analog loop filter. The RX SNR after demodulation will be degraded as well as sensitivity if the RX loop delay of $t_{loop}$ become larger. Referring to the system behavioral simulations in [7], the SNR of the RX will be degraded much and up to 6 dB while the $t_{loop}$ is varied 30% from the optimum design value. As discussed before, the $t_{loop}$ is always dominated by the delay of the integrated analog baseband filter since its low cut-off bandwidth of sub-MHz to several-MHz at different data rate of Mb/s. The sharp filtering feature is needed to design for the loop filter to reduce the interference or blockers residue at baseband part which will increase the loop delay and thus degrade the sensitivity [4, 7].

To ease the loop filter design and maintain the sensitivity of the RX, we reuse the MEMS-based oscillator working at FSK mode as the LO in the proposed phase-tracking RX to achieve super interference resilience. As shown in Fig. 2, the interferences or blockers are still strong after the FSK matched filter and LNA. Assuming we design the same baseband blocks, when we use the normal DCO FSK signals as the LO, the SNR of the baseband will be degraded without additional filtering. Compared to the normal DCO FSK LO, the MEMS-based FSK LO has the better side-lobe suppression and in-band rejection inherently which is benefit from the high-Q (~1000) MEMS

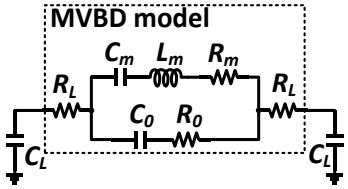


Fig. 3. MEMS resonator MVBD equivalent circuit

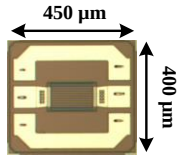


(a)

| Elements | Values |
|---|---|
| $L_m$ (µH) | 2.59 |
| $C_m$ (fF) | 11.8 |
| $R_m$ (Ω) | 36.5 |
| $C_0$ (fF) | 195.3 |
| $R_0$ (Ω) | 9 |
| $R_L$ (Ω) | 1.8 |
| $C_L$ (fF) | 121 |

(b)

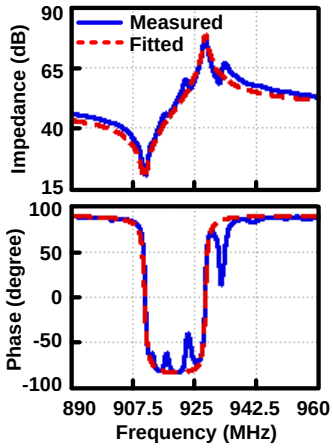


(c)

Fig. 4. (a) The microphotography of a MEMS resonator; (b) MBVD model parameters and (c) measured parallel impedance response and model-fitted impedance.

resonators. As shown in Fig. 2, the side-lobe suppression and in-band rejections of the implemented MEMS-based FSK LO are 30 dB and 28 dB, respectively, which are 16 dB and 18 dB better than the normal DCO FSK LO. Therefore, better interference /blocker suppressing as well as sensitivity could be achieved without shaping analog filter or additional digital filtering after the analog baseband.

## III. MEMS-BASED FAST SWITCHING TRANSMITTER

The proposed prototype of the implemented MEMS-based FSK/OOK transmitter is shown in Fig. 1, a preliminary work on FSK transmitter has been published in [14]. To ensure dual-frequency output with scalable modulation index, the binary FSK/OOK modulator leveraging dual MEMS resonators is used. The FSK/OOK modulator can be switched by the input data directly, achieving adaptive tracking. Subsequently, the output is fed into a driving amplifier (DA) and it is transmitted by the following antenna. Benefitting from the high-Q MEMS resonators, significant side-lobe suppression is achieved by the system, resulting in large leakage reduction without additional filtering after the DA [8].

### A. *MEMS resonator*

The MEMS-based oscillators have shown promising advantages, which exhibit measured Q is around 1000 under operating frequencies of the GHz range [13-19]. A MEMS resonator can be modeled using a RLC tank circuit [15]. The Modified Butterworth-Van Dyke (MVBD) equivalent circuit of an MEMS resonator together with the capacitive loading $C_L$ is shown in Fig. 3. $C_o$, $R_o$ and $R_L$ represent the resonator's static capacitance and resistance from the routing metals. $L_m$, $C_m$ and $R_m$ are the motional parameters that model the resonator behavior operating near the resonant frequency. $C_L$ represents the parasitic capacitance due to resonator pads, oscillator circuits and packaging. Both series and parallel resonance can be exploited in a MEMS resonator. At series ($f_s$) or parallel ($f_p$) resonant frequency, the resonator will exhibit the lowest resistance ($R_s$) or the highest resistance ($R_p$) respectively. The resonant frequencies could be derived from (1) and (2) as follows

$$f_s = \frac{1}{2\pi}\sqrt{\frac{1}{L_m C_m}}\ , \tag{1}$$

$$f_p = f_s\sqrt{1+\frac{C_m}{C_0+0.5C_L}}\ . \tag{2}$$

For the cross-coupled structure, parallel resonance with large $R_p$ is chosen to provide larger loop gain at $f_p$. A larger $R_p$ also helps to reduce the power needed to start the oscillation.

In this work, we fabricated the Plate-Mode piezoelectric MEMS resonator by an in-house 200-mm wafer process line. The details of processing steps are illustrated in [14, 20-23]. On the both top and bottom sides of the 2.0-µm-thick piezoelectric Scandium doped Aluminium Nitride (ScAlN) layer, there are two sets of 0.2-µm-thick Molybdenum interdigitated electrodes (Mo IDEs), respectively. To meet the cross-sectional requirements of the Plate-Mode resonator and ensure the efficient connection to its IDEs, the polarities are set as opposite between the adjacent IDEs along the lateral direction and the IDEs on the other sides of the ScAlN layer at the same lateral direction [20-22]. Based on such an IDE configuration and resonator dimensions, the plate-wave can be generated giving rise to a high Q. Consequently, the Q performance of the oscillator is enhanced. Additionally, more resonators could be bonded to this hybrid modulator on PCB, then the desired ones can be selected through on-chip switches for multi-band operation. Fig. 4(a) shows a fabricated MEMS die photo and the dimension is 450 µm × 400 µm. By introducing the metal resistance and substrate loss and using the modeling method described above, the derived MEMS resonator equivalent circuit parameters and impedance plot including the model-fitted impedance are shown in Fig.4 (b) and (c). The Q factor at the parallel resonance frequency $f_p$ is 983. These parameters will be taken into consideration while designing the MEMS-based oscillator circuit.

### B. *MEMS-based FSK/OOK modulator*

As designed in Fig. 5, the dual-MEMS resonators can be driven symmetrically by the oscillator with differential topology. The FSK/OOK modulator operates with a switched MEMS resonator oscillator and can ensure fast switching by fast transition control. The dual-MEMS resonators in the oscillator are placed in parallel. The complementary switches S and SN will determine one branch of cross-coupled pairs ($M_{N1}$/$M_{N2}$ or $M_{N3}$/$M_{N4}$) to get the corresponding MEMS resonators connected to the tail current and the active load. The switch control signals S and SN is dynamical signal which are generated by the control logical illustrated in Fig. 5. The S and SN are the complementary signal of DATA_IN when the modulator is working as FSK mode (FSK/OOK_EN=1). On

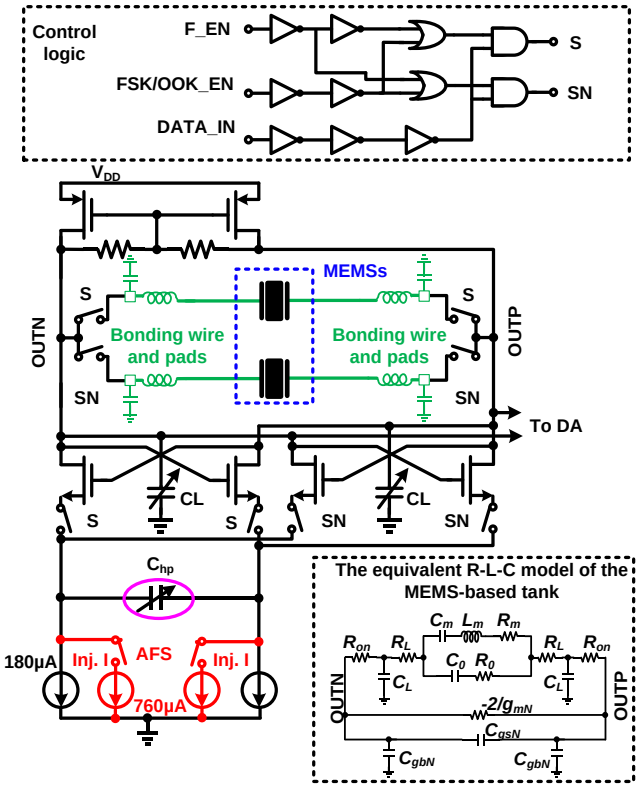


Fig. 5. The schematic of the MEMS-based OOK/FSK modulator.

OOK mode (FSK/OOK_EN=0), there are two cases: the S is the same with DATA_IN and the SN is always 0 when the F_EN=0, vice versa. Parallel capacitive loading will be introduced by the complementary switches when they are turned off, and series resistance will be induced when they are turned on. The former could impact the resonant behavior such as frequency shifting while the latter would reduce the loaded quality of the resonant tank. We choose the switch size to be 20 μm/280 nm to minimize the capacitive loading while maintaining reasonably small switch on resistance. The equivalent R-L-C model of the MEMS-based tank of the modulator is shown in Fig. 5. As shown in the figure, the $R_{on}$ is the on-resistor when the switch is on to connect the MEMS resonator and the modulator. Resistor of $-2/g_{mN}$ is the negative resistance generated by the cross-coupled pair, $C_{gsN}$ and $C_{gbN}$ are the parasitic of the cross-coupled pair. The parasitic will degrade the Q of the MEMS-based tank. In simulation, the Q of the modulator tank is only 373 while the Q of the MEMS block (disconnected to the modulator) is 983. Frequency tuning of the modulator is implemented by a 3-bit digitally controllable capacitor bank CL at the output nodes to remove frequency offset between TX and RX for FSK demodulation. As shown in Fig. 5, the frequency tuning range is from 925.4 MHz to 920.3 MHz when the CL is varied from 0.1 pF to 1pF.

As mentioned earlier, differential oscillator architecture with cross-coupled pair is chosen because of its power efficient benefit. Active load with common-mode feedback (CMFB) is leveraged to stably self-bias the oscillator's output to 0.6 V while providing high loaded Q. Nevertheless, it should be noted that the resonator presents a high impedance near to DC and low frequencies due to the $C_0$, as shown in Fig. 3 of MVBD

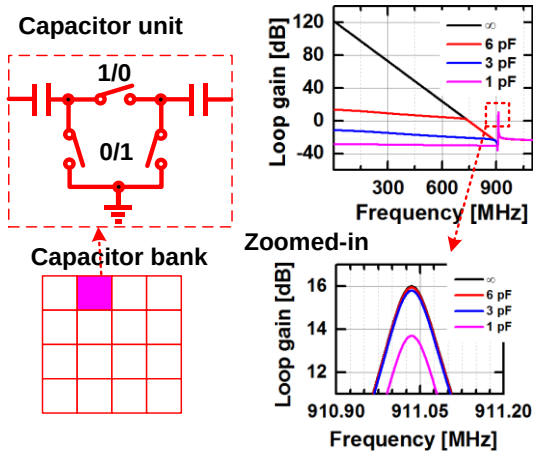


Fig. 6. The implemented capacitor bank of $C_{hp}$ and the simulated loop gain of the oscillator of 911 MHz with different $C_{hp}$.

equivalent circuit. With the cross-coupled structure, a broadband negative resistance is provided; however, the oscillator is prone to be latched up to DC or lower frequencies rather than oscillating at the resonant frequency [14, 23]. To resolve this issue, the tail current is split into two symmetric branches and is coupled to the cross-coupled pairs via a capacitor $C_{hp}$, as shown in Fig. 5.

At lower frequency, the cross-coupled pair transistors will see large source degeneration resistance and exhibit very large negative resistance. At higher frequency, the source terminals of cross-coupled pair would be shorted by the capacitor, producing an AC ground to exhibit small negative resistance. The differential impedance seen from the drain of the cross-coupled pair of $M_{N1}$ and $M_{N2}$ or $M_{N3}$ and $M_{N4}$ is [5]:

$$Z_{cross} = -\frac{2}{g_{mN}}\left(1+\frac{g_{mN}}{2j\omega C_{hp}}\right), \quad (3)$$

where $g_{mN}$ is the transconductance of the cross-coupled transistor pair $M_{N1}$ and $M_{N2}$ or $M_{N3}$ and $M_{N4}$, and $\omega$ is the resonance angular frequency. From (3), the cross-coupled circuits provide a negative resistance of $-2/g_{mN}$ at high frequency since the $Z_{cross}$ could be reduced at low frequency by $C_{hp}$. When $C_{hp}$ is large, it is possible to cause parasitic oscillation at low frequency due to the low frequency instability caused by the inductive nature of capacitive degenerated cross-coupled pair in parallel with its parasitic cap and the static capacitance of the parallel MEMS resonators. The parasitic oscillation would occur while the loop gain exceeds 0 dB based on the Barkhausen's criterion [5, 23]. By reducing the value of $C_{hp}$, the parasitic oscillation effect can be suppressed. With the reduced $C_{hp}$, the gain at the low frequency will be attenuated greatly, and it will increase the negative resistance pole frequency from (3), which decreases the loop gain at the required resonance frequency of the MEMS resonator. Thus, the choice of $C_{hp}$ will impact the DC stability and high frequency loop gain for the efficient oscillation. Fig. 6 illustrates the loop gain variation with different $C_{hp}$ at around 911 MHz. As shown in the figures, to remove the low frequency oscillation and keep the relatively high loop gain at the GHz frequency, the $C_{hp}$ could be chosen as several pF. Furthermore, there are two branches of cross-coupled pair in this design, the value of the $C_{hp}$ is tunable to maintain oscillation as FSK generation and adapts to MEMS resonators with different $C_0$,

This article has been accepted for publication in IEEE Journal of Solid-State Circuits. This is the author's version which has not been fully edited and content may change prior to final publication. Citation information: DOI 10.1109/JSSC.2022.3211907



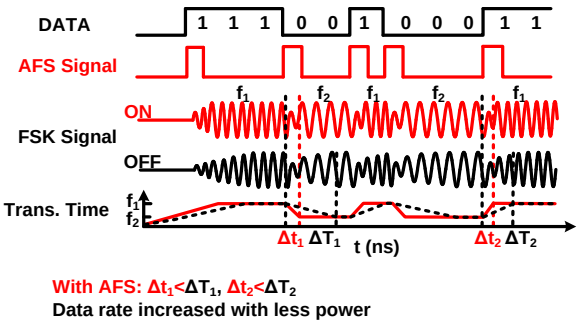


Fig. 7. AFS operation for MEMS-based modulator.

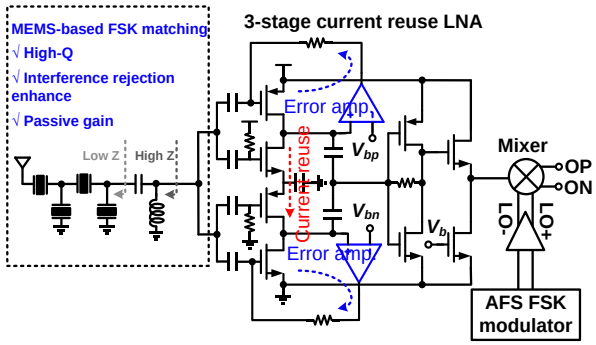


Fig. 8. The schematic of the proposed primary RXFE.

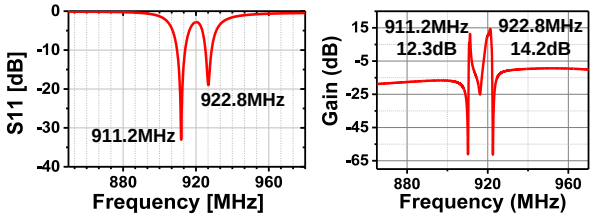


Fig. 9. (a) Simulated S11 and (b) gain of the external matching network with MEMSs.

as illustrated in Fig 3. To enlarge the loop gain, the size of the cross-coupled transistors (*W/L*, the width over length) could be set large to increase the $g_{mN}$. However, the parasitic capacitance will be increased with the increase of the transistor's size, which would pull down the sense impedance and in turn attenuate the loop gain of the oscillator. In this design, two different sets of cross-coupled pairs with the *W/L* of 80 µm/60 nm and 96 µm/60 nm are chosen for different MEMS resonators. In addition, the capacitive source degeneration $C_{hp}$ can also help to mitigate the capacitive loading at the oscillator output [5, 14, 23]. $C_{hp}$ is designed as a 5-bit capacitor bank, covering from 1 pF to 4.5 pF.

As discussed before and illustrated in Fig. 7, an adaptive current injection scheme is employed to enable the maximum transmission data rate of 6 Mb/s while only consumes sub-mW power consumption. By simulation, the transition time is reduced continuously from 160 ns to 82 ns when the injection current is varied from 100 µA to 700 µA. However, the transition time is increased while the injection current is injected from 700 µA to 800 µA. The main reason is the loop gain of the oscillator is dropped with too large current while the size of the cross-coupled transistor is not adjusted correspondingly. To speed up the transition consuming less average power, an optimized 760-µA current is injected into the oscillator via a pulse duration of ~50 ns at start edge of each modulated data, low of 0 or high of 1. Then, the oscillator would maintain a stable oscillation with a 180-µA current. Based on the technique, during FSK frequency transition, the rising time and falling time would be significantly reduced to almost half. On average, only 480 µA current is consumed by the oscillator.

To remove the loading effect for the modulator, a 3-stage cascaded DA is adopted to drive the antenna directly. Inverter-based structure is used to maximize efficiency. To minimize the loading to the MEMS-based modulator, small transistor size is used for the first stage. In the last stage, an output power of -10 dBm by setting the NMOS of 10 µm/65 nm and the PMOS of 20 µm/65 nm and it will ensure the targeted transition distance.

## IV. MEMS Based Receivers

In the section, the circuit of primary FSK RX and WuRX building blocks, including the RX front end, analog baseband and zero power RF ED are descripted in details.

### A. *RX front end*

Fig. 8 shows the proposed primary RX front end (RXFE) circuits following a FSK matched filter and matching network. The FSK matched filter is implemented by 4 MEMS resonators to provide >30 dB in-band interference and >40 dB out-of-band blocker/ interference suppression. Co-designed with a passive matching network implemented with a 106 nH inductor and a 1.2 pF capacitor to LNA, which also provides a ~13 dB passive gain by impedance transformation. The simulated input reflection coefficient $S_{11}$ of the RX with MEMSs is illustrated in Fig. 9 (a). There are two peak frequencies are located in 911.2 MHz and 922.8 MHz corresponding to the resonance frequencies of the MEMS resonators. The simulated passive gain of the external matching network is shown in Fig. (b), the peak passive gain is 14.2 dB at 922.8 MHz.

To save power, the current-reused LNA consisting of two stacked inverter-based amplifiers is employed in the first stage to form the dual LNAs to achieve an additional 6 dB gain increment. To make the transistors working in the inversion region, two error amplifiers are used in the feedback to provide DC point for the amplifier. Thereafter, the output current of the two amplifiers feeds into the second stage where the two signals are superimposed together. The third stage applied a source follower to drive the input capacitance of the subsequent stage. Overall, the LNA exhibits 20 to 40 dB gain and 28.9 dBµV input-referred noise while consuming ≤102 µW power. The simulated noise figure (NF) and output 1-dB compression point (OP-1dB) are 6.2 to 6.7 within the ISM-915 MHz band and -14.6 dBm, respectively.

After the LNA, a single-balanced active mixer consuming 15.2 µW power consumption is adopted. Benefit from the inherent good side-lobe suppression of the MEMS-based modulator, through coherent correlation, the in-band and out-of-band interference/noise can be further suppressed by using side-lobe suppression LO to achieve better sensitivity without high-order shaping analog filter or additional digital filtering after the analog baseband.

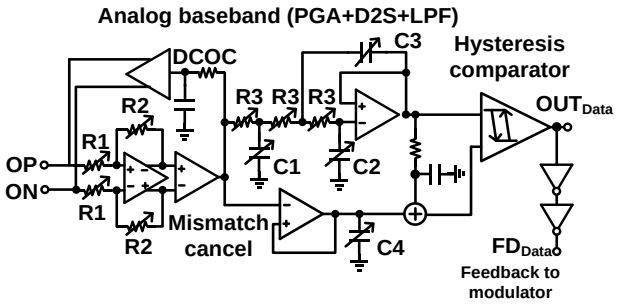


(a)

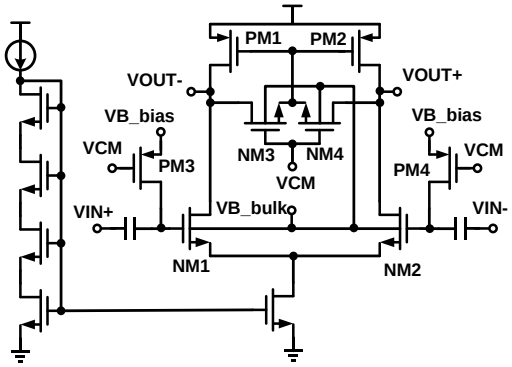


(b)

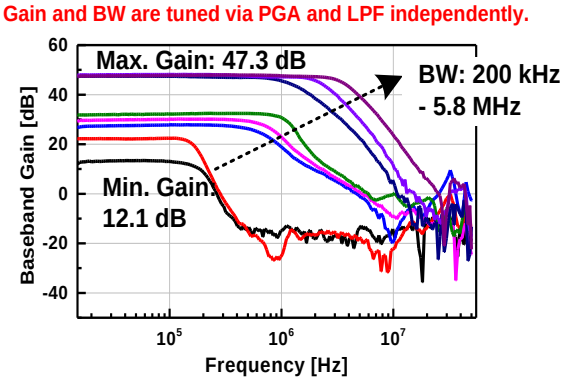


(c)

Fig. 10. (a) The diagram of the analog baseband, (b) the schematic of the baseband amplifier and (c) the measured analog baseband bandwidth and gain response with different setting.

## B. *RX analog baseband circuits*

After the mixer, the analog baseband (ABB) is integrated as a 2-stage PGA with DCOC, a 3rd-order elliptic LPF and a hysteresis comparator, as shown in Fig. 10(a). The gain and filtering stages are used to attain configurable gain and bandwidth by the control words (CWs), 6-bit CWs for bandwidth changing and 3-bit CWs for gain changing to meet the loop requirement for different data rate. Due to good linearity and sensitivity, a prototype of passive ladder filter is designed as the active filter design reference. An active RC LPF is implemented basing on the passive prototype. A fully differential amplifier is used to form the PGA and filter, as shown in Fig. 10(b). To ensure the PGA and LPF to work at low power supply of sub-1 V, body biasing technique [22] is adopted to control the $V_{TH}$ variation of the transistors NM1, NM2, NM3 and NM4. In order to get the necessary bandwidth while the amplifier is working at low power, the size of transistors are design to small size but it exhibits large DC offset. To solve it, an AC-coupled circuit using transistors of PM3 and PM4 as pseudo-resistors of MΩ resistors, which could make the high-pass cutoff frequency as lower as <50 kHz. Similarly, transistors NM3 and NM4 are used as large active resistors for CMFB to maintain the output DC operation point. A 3-bit resistor array (R1 and R2) for PGA and a 6-bit capacitor/resistor arrays (R3, C1, C2 and C3) for LPF are tuned via an integrated serial peripheral interface (SPI) to control the gain and bandwidth for different data rates. In Fig. 10 (c), these stages provide a tunable bandwidth from 0.3 to 6 MHz, and a configurable gain range from 13 to 49 dB with a gain step of 3 dB to support variable data rates.

After the LPF, a hysteresis comparator is adopted to demodulate the data. A feedforward frequency mismatch cancellation path is realized by an active RC circuit with lower cut-off frequency, and which generates a reference input to the comparator. The comparator output will then be sent to the binary FSK modulator to complete the phase-tracking RX. Overall, the FSK RX consumes 232μW, excluding the FSK modulator.

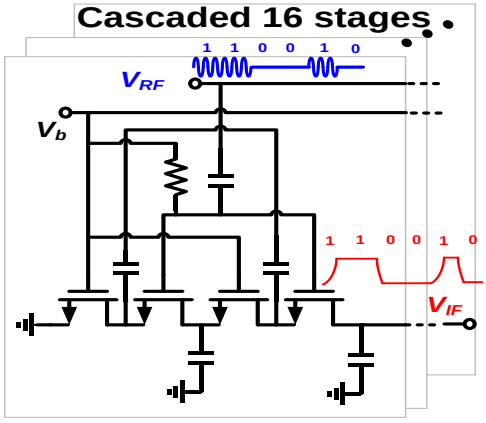


Fig. 11. The proposed zero-power RF ED for WuRX

## C. *WuRX and zero-power ED*

As shown in Fig. 1, an OOK WuRX is implemented with a zero-power ED while reusing the LNA at low power mode and the analog baseband of the primary RX. Due to the lower power and lower gain of the LNA, the simulated NF of the LNA is 6.9 to 7.5 within the ISM-915 MHz band which is a ~0.8 dB degradation in the OOK path. The received signal is first amplified by the LNA and then detected by a multistage ED which achieves a certain voltage gain. Thereafter, its output is fed into the analog baseband to get the demodulated data as a wake up receiver working at <200 kbps.

The proposed zero-power ED is shown in Fig. 11, 16 stages of a four-stage self-mixer cell [24] are adopted to minimize the power further. There are two different working modes for the transistors in the four-stage self-mixer. The amplified RF signal $V_{RF}$ after LNA is AC coupled to the source and gate nodes in mode 1 and $V_{RF}$ is AC coupled to the drain node in mode 2. The DC biases for both modes are could be $V_{GB}=V_b$ and $V_{DB}=V_{SB}=V_{DS}=0$, respectively. As discussed in [22], thanks to the same polarity of the outputs for both modes, the average

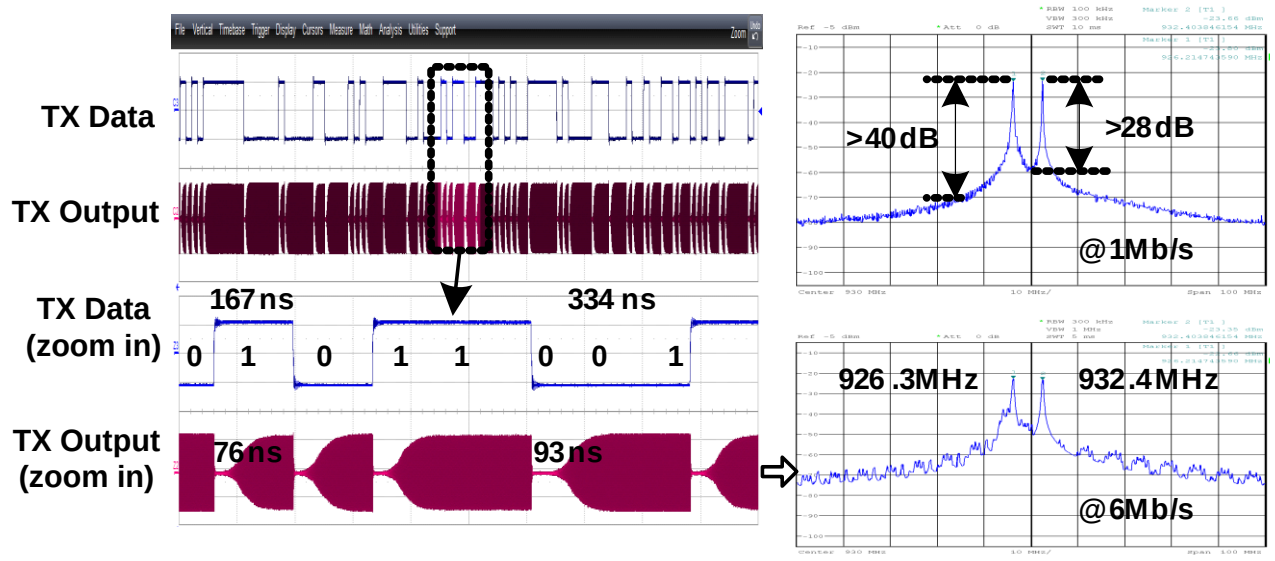


Fig. 13. Measured TX performance of time domain response and spectrums.

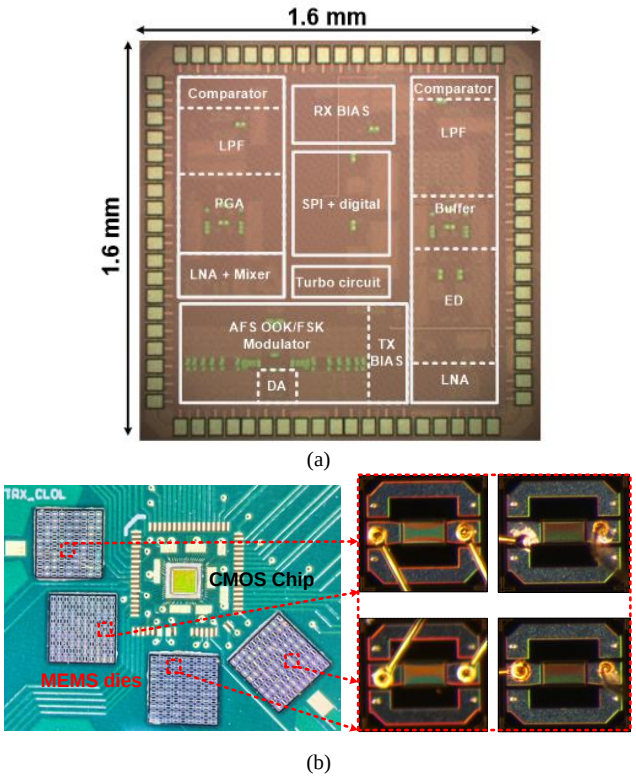


Fig. 12. (a) The Die and (b) chip on board microphotograph.

conversion gain constant of $k_{ed,1}=1/(2nV_t)$ could be added for multistage implementation, where $n$ is the coefficient for the sub-threshold slope and $V_t = k_BT/q$ is the thermal voltage with $k_B$ Boltzmann's constant, $T$ is the absolute temperature, and $q$ is the electron charge. For N-stages, the baseband output of ED is then

$$v_{IF} = k_{ed} {v_{RF}}^2 = N \frac{(v_{RF})^2}{2nV_t} \quad (4)$$

where $k_{ed} = N/(2nV_t)$ is conversion constant. To trade-off the area and gain, we used 16 stages of the four-stage self-mixer cell as the RF ED. The whole WuRX consumes 86 µW at 1V power supply with the data rate up to 200 kb/s, and achieves sensitivity of -71 dBm.

## V. Implementation and Experiments

The transceiver has been implemented in a 65-nm CMOS process. To minimize the bonding parasitic, the CMOS chip and MEMS die are wire-bonded directly onto a print circuit board (PCB) as the evaluation prototype. The microphotograph of the CMOS chip, the chip in package and the evaluation board are shown in Fig. 12. The chip area is 1.6 mm × 1.6 mm including all IO pads. Deep N-wells or metal grounded shielding are employed as shielding for the RF sensitive building blocks to isolate or degrade the substrate noise coupling. In this test prototype, a simply mechanic SPDT switch on PCB board is used to select the connection the antenna between RX and TX manually.

The Keysight 33600A series waveform generator is used to generate the internal pseudo-random data pattern of PN7, which is used for the modulation TX data. The measured FSK waveform and spectrum of the TX output at 1 Mb/s and 6 Mb/s are shown in Fig. 13, and the output power is up to -11.2 dBm. The FSK signals peak at 926.3 MHz and 932.4 MHz and the frequency deviation of FSK is 5.9 MHz. As shown in the spectrum of the TX output, the side-lobe rejection is larger than 40 dB and in-band rejection is higher than 28 dB, which is benefited from the high-Q MEMS resonators. By leveraging the AFS technique, the transition time of the modulator with AFS are found to be 76 ns and 93 ns respectively. In contrast, the transition time are 289 ns and 352 ns without current injection. At 1-MHz offset, the measured phase noise is -139.7 dBc/Hz, -140.2 dBc/Hz, and -139.3 dBc/Hz at 912.5 MHz, 926.3 MHz and 932.4 MHz, respectively (in Fig. 14). Compared to the simulation results, there is a 6-8 dB degradation due to the bonding-wire parasitic. In Fig. 15, a clear FSK eye diagram is observed with a FSK error of less than 2.17%.

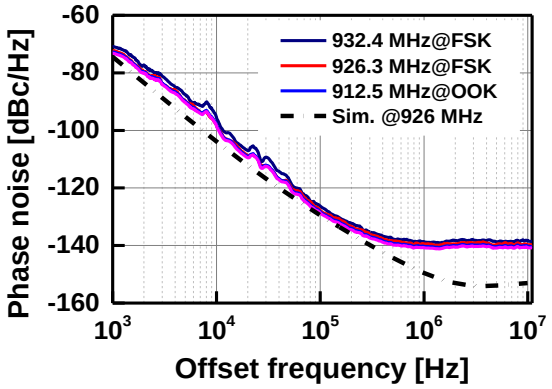


Fig. 14. Measured PN at different frequencies and simulated PN.

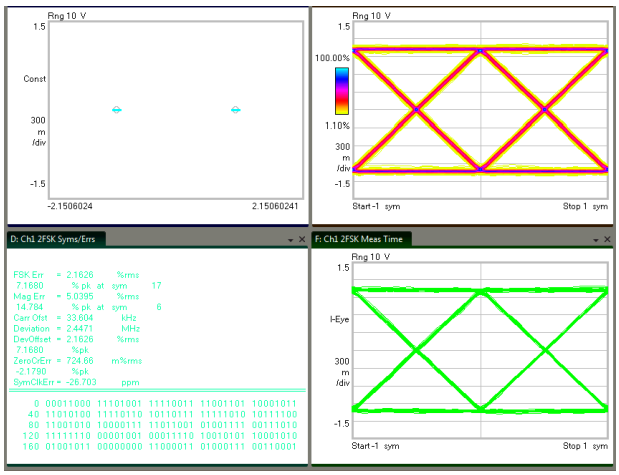

Fig. 15. Measured TX FSK performance and the FSK error less than 2.17% at 6 Mbps data rate.

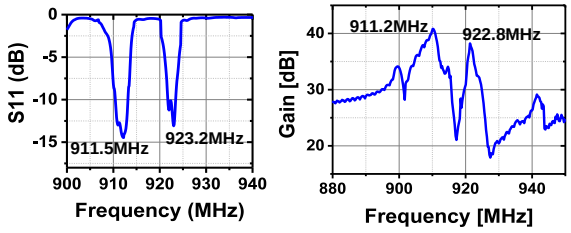


Fig. 16. Measured S11 and gain of the LNA with MEMSs

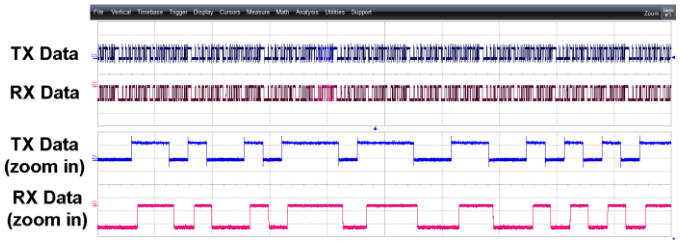


Fig. 17. Measured typical FSK demodulation results @ 2 Mb/s data rate

The measured gain of the LNA with MEMSs is shown in Fig. 16, there are two peaking distinct frequencies, 911.2 MHz and 922.8 MHz of the FSK matched filter. By measuring output of LNA, the measured passive gain provided by the passive matching network is 12.1 dB and the total gain with LNA is 38-41 dB. There is a maximum 2.1 dB degradation of the passive gain mainly contributed by bonding wire and parasitic on the

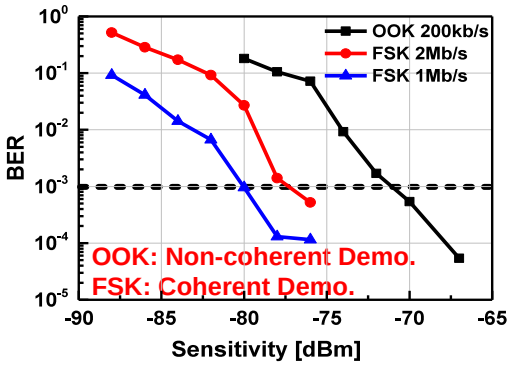


Fig. 18. Measured sensitivity at different data rate and demodulation mode.

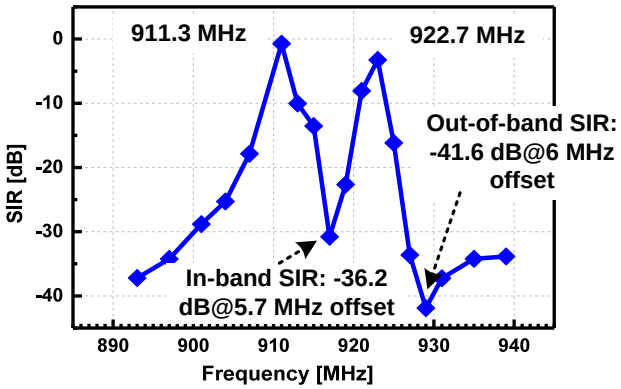


Fig. 19. Measured SIR performance

PCB To illustrate the demodulation of the RX, a pseudo-random data sequence modulated FSK signal generated by the TX which is fed into the RX after attenuation, and the modulated and demodulated data sequence is show in Fig. 17. FSK-modulated RF carriers with 1 Mb/s and 2 Mb/s pseudo-random sequences were fed into the receiver to measure the bit error rate (BER) with varying input signal power, as shown in Fig. 18. The sensitivity of -78.2 dBm and -77.5 dBm are achieved at BER of $< 10^{-3}$. The OOK-demodulation when input a RF carrier modulated by a 200 kb/s pseudo-random code was also measured, and a sensitivity of -71 dBm while BER of $< 10^{-3}$ is achieved. The signal-to-interference ratio (SIR) to maintain a BER of $10^{-3}$ is measured with the input signal at -74.5 dBm (3 dB higher than the sensitivity) at 2 Mb/s. In Fig. 19, the in-band and out-of-band SIR are as good as -36.2 dB@5.7 MHz offset and -47.1 dB@6 MHz offset, respectively.

A typical wireless link testing setup for the prototyped MEMS based FSK transceiver system is demonstrated in Fig. 20. The photograph of the test setup is shown in Fig. 20 (a). Two chips are working as TX mode and RX mode, respectively. The antenna is commercial ISM-915 antenna (P/N 0915AT43 A0026) for small form factor applications and the average gain is -4 dBi. The data rate is 1 Mb/s and the output power of the TX is -12 dBm. The chip to chip results are shown in Fig. 20 (b), and the transmission distance could be up to about 5.5 m. Fig. 21 shows the breakdown of the power consumption of each key blocks. Due to the direct modulation for high data rate, the modulator consumes 61% power. According the simulation results, the transmitter only consumes 4.8 μW at an average data rate of 100 kb/s when the modulator works with a duty-

TABLE I.

PERFORMANCE OF THE MEMS-BASED TRANSCEIVER AND COMPARISON

| | | This work | | H. Bialek, ISSCC 2021 | L. Chuo, ISSCC 2017 | Y. Shi, ISSCC 2019 | M. Song ISSCC 2020 | J. Bae, JSSC 2011 | D. Ye, ISSCC 2016 | X. Huang, ISSCC, 2012 | A. Paidimarri, JSSC 2013 |
|---|---|---|---|---|---|---|---|---|---|---|---|
| Technology | | **65nm CMOS** | | 65nm CMOS | 180nm CMOS | 65nm CMOS | 40nm CMOS | 180nm CMOS | 65nm CMOS | 90nm CMOS | 65nm CMOS |
| Operating Frequency | | **911.2 MHz and 922.8 MHz** | | 0.75-1 GHz | 915 MHz | 2.4 GHz | 400 MHz | 920 MHz | 915 MHz | 915 MHz | 2.4 GHz |
| Modulation | | **OOK** | **FSK** | CW/ QPSK | PPM | GFSK | GFSK | FSK | BPSK | FSK/OOK | OOK/BPSK |
| Demodulation | | **Open-loop (ED*)** | **Closed-loop (PT*)** | Open-loop (N-Path) | Open-loop (ED*) | N.A. | Closed-loop (PT*) | Open-loop (ED*) | TX-Ref. & Shifted Limiter | Open-loop (ED*) | N.A. |
| TX Output Power | | **-11.2 dBm** | | N.A. | -2 dBm | -8.4 dBm | -6 dBm | -10 dBm | N.A. | -6 dBm | -10 dBm |
| Off-chip Components | Type | **MEMS / L / C** | | Hybrid coupler / L | 3D Magnetic Antenna / C | Planar Loop Antenna | Planar Antenna. | L | L | SAW / L | FBAR |
| | Size | **450 × 400 µm² / 0603 / 0603** | | 14 × 8.9 mm² / N.A. | 3 × 3 mm² / N.A. | 3.5 × 3.5 mm² | 3.5 × 3.8 mm² | N.A. | N.A. | N.A. / N.A. | N.A. |
| | No. | **6 / 1 / 1** | | 1 / 1 | 1 / 1 | 1 | 1 | 5 | 1 | 1 / 1 | 3 |
| Data Rate | | **200 kb/s** | **6/2 Mb/s#** | 10 kb/s | 30.3 kb/s | 1Mb/s | 200 kb/s | 5 Mb/s | 10 kb/s | 10 kb/s | 1 Mb/s |
| RX Sensitivity | | **-71 dBm** | **-77.5 dBm** | -86 dBm | -93 dBm | N.A. | -90 dBm | -73 dBm | -76 dBm | -83 dBm | N.A. |
| SIR | | **-36.2 dB@5.7 MHz -47.1 dB@6 MHz##** | | -35 dB@ 5MHz | N.A. | N.A. | N.A. | -20 dB@ 50 MHz | -2.5 dB@ 1 MHz | -19 dB@ 8 MHz | N.A. |
| Supply Vol. | | **1 V** | | 0.7 V | 4/2/1.2 V | 1.2 V | 1 V | 0.7 V | 1 V | 1 V | 0.7/1 V |
| Power | TX | **0.64 mW** | | N.A. | 2 mW | 0.61 mW | 3.1 mW | 0.7 mW | N.A. | 0.9 mW | 0.44 mW |
| | RX | **86 µW** | **0.52 mW** | 0.44 mW | 1.85 mW | N.A. | 1.5 mW | 0.42 mW | 0.135 mW | 0.12 mW | N.A. |
| Energy Per Bit | TX | **107 pJ/b** | | N.A. | 66000 pJ/b | 610 pJ/b | 15500 pJ/b | 140 pJ/b | N.A. | 90000 pJ/b | 440 pJ/b |
| | RX | **430 pJ/b** | **260 pJ/b** | 4400 pJ/b | 29000 pJ/b | N.A. | 7500 pJ/b | 84 pJ/b | 13500 pJ/b | 12000 pJ/b | N.A. |
| RX FoM** | | **164** | **173** | 164 | 165 | N.A. | 168 | 173 | 154 | 162 | N.A. |

* PT: Phase-tracking; ED: Envelope Detection. # TX data rate is 6 Mb/s and FSK RX data rate is 2 Mb/s
## -36.2 dB of in-band SIR @ 5.7 MHz offset and -47.1 dB of out-of-band SIR@6 MHz offset
** RX FoM= -Sensitivity-10×log10(Power/Data Rate)

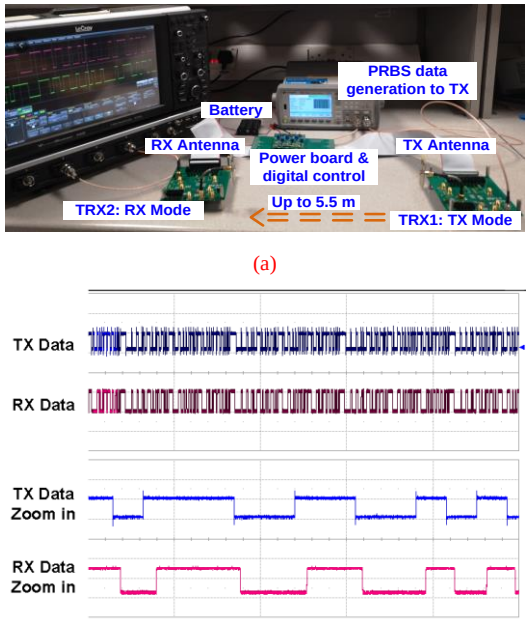


Fig. 20. (a) The typical testing setup of wireless link for the prototyped MEMS based FSK transceiver system and (b) measured FSK demodulation results @ 1 Mb/s data rate

cycle ratio of 1.6%, which is a trade-off for the ULP IoT application with different requirements.

The performance is summarized and compared with the other published state-of-the-art in Table I. Compared with literature, the proposed RX has the best SIR performance thanks to the co-design with FSK filter and LNA. Also, the

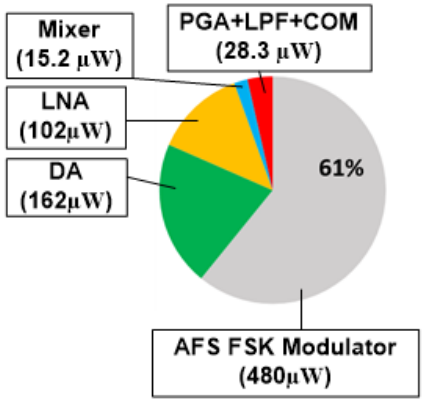


Fig. 21. Power breakdown of the FSK TRX

proposed FSK TX achieves over 1.5× better energy efficiency at 1 V supply while having over 1.2× higher data rate of 6 Mb/s and the FSK RX demonstrates the best FoM with the sensitivity of -77.5 dBm.

## VI. CONCLUSION

This article presents an ULP MEMS-based phase-tracking FSK TRX with an embedded ED OOK WuRX in 65 nm CMOS. The TX using an adaptive fast switching binary MEMS-based modulator generates FSK/OOK signals of ISM-915 MHz with -11.2 dBm output power, supporting up to 6 Mb/s. By sharing the modulator, the RX exhibits -36.2 dB in-band SIR, -77.5 dBm sensitivity at BER of $10^{-3}$ at 2 Mb/s. The TX, FSK RX and

WuRX consume 642 µW@6 Mb/s, 520 µW@2 Mb/s and 86 µW@200 kb/s at 1V power supply which achieve energy efficiency 107 pJ/b, 260 pJ/b and 430 pJ/b respectively.

## REFERENCES


[1] L. Chuo et al., "A 915MHz Asymmetric Radio Using Q-Enhanced Amplifier for a Fully Integrated 3×3×3mm3 Wireless Sensor Node with 20m Non-Line-of-Sight Communication," *ISSCC*, pp. 132–133, Feb. 2017.

[2] P. P. Wang et al., "A 220µW -85dBm Sensitivity BLE-Compliant Wake-up Receiver Achieving -60dB SIR via Single-Die Multi- Channel FBAR-Based Filtering and a 4-Dimentional Wake-Up Signature, " *ISSCC*, pp. 440–441, Feb. 2019.

[3] Y.-H. Liu, et al., "A 770pJ/b 0.85V 0.3mm2 DCO-Based Phase-Tracking RX Featuring Direct Demodulation and Data-Aided Carrier Tracking for IoT Applications," *ISSCC*, pp. 408-409, Feb. 2017.

[4] M. Ding et al., "A 0.8 V 0.8 mm2 Bluetooth 5/BLE Digital-Intensive Transceiver with a 2.3 mW Phase-Tracking RX Utilizing a Hybrid Loop Filter for Interference Resilience in 40nm CMOS," *ISSCC*, pp. 446–448, Feb. 2018.

[5] H. Bialek et al., "A 0.75-to-1GHz Passive Wideband Noise-Cancelling 171µW Wake-Up RX and 440µW Primary RX FE with -86dBm/10kb/s Sensitivity, 35dB SIR and 3.8dB RX NF," *ISSCC*, pp. 308-309, Feb. 2021.

[6] Y. Shi et al., "A 606µW mm-Scale Bluetooth Low-Energy Transmitter Using Co-Designed 3.5×3.5mm$^2$ Loop Antenna and Transformer-Boost Power Oscillator," *ISSCC*, pp. 442-443, Feb. 2019.

[7] M. Song et al., "A 3.5mm×3.8mm Crystal-Less MICS Transceiver Featuring Coverages of ±160ppm Carrier Frequency Offset and 4.8-VSWR Antenna Impedance for Insertable Smart Pills," *ISSCC*, pp. 474-475, Feb. 2020.

[8] J. Bae et al., "A Low Energy Injection-Locked FSK Transceiver with Frequency-to-Amplitude Conversion for Body Sensor Applications," *IEEE JSSC*, Vol. 46, NO. 4, pp. 928-937, April 2011.

[9] D. Ye et al., "An Ultra-Low-Power Receiver Using Transmitted-Reference and Shifted Limiters for In-Band Interference Resilience," *ISSCC*, pp. 438-439, Feb. 2016.

[10] D. Ye et al., "A 915 MHz 175 µW Receiver Using Transmitted-Reference and Shifted Limiters for 50 dB In-Band Interference Tolerance," *IEEE JSSC*, Vol. 51, NO. 12, pp. 3114-3124, Dec. 2016.

[11] X. Huang *et al.*, "A 915MHz 120µW-RX/900µW-TX Envelope-Detection Transceiver with 20dB In-Band Interference Tolerance," *IEEE ISSCC*, pp. 454-455, Feb. 2012.

[12] X. Huang *et al.*, "A 915 MHz, Ultra-Low Power 2-Tone Transceiver With Enhanced Interference Resilience," *IEEE JSSC*, Vol. 47, NO. 12, pp. 3197-3207, Dec. 2012.

[13] J. Tao *et al.*, "A 5-pJ/bit OOK Transmitter Using MEMS-based RF Oscillator for IoT Application in 180-nm CMOS," *IEEE Microwave and Wireless Components Letters*, Vol. 31, No. 10, pp. 1158-1161, Oct. 2021.

[14] K. Tang *et al.*, "A 75.3 pJ/b Ultra-Low Power MEMS-based FSK Transmitter in ISM-915 MHz Band for Pico-IoT Applications," *IEEE International Symposium on Circuits and Systems (ISCAS)*, May, 2021.

[15] C. Zuo, J. Van Der Spiegel, and G. Piazza, "1.05-GHz CMOS Oscillator based on Lateral-Field-Excited Piezoelectric AlN Contourmode MEMS resonators," *IEEE Transactions on Ultrasonics, Ferroelectrics and Frequency Control*, vol. 57, pp. 82-87, 2010.

[16] Y. Zhu et al, "A high-impedance dual-mode SAW resonator for ultra low powerand high data rate FSK modulator," *Sensors and Actuators A: Physical*, 220 (2014), pp 188-193.

[17] C. Zuo, N. Sinha, J. Van der Spiegel, and G. Piazza, "Multifrequency Pierce Oscillators Based on Piezoelectric AlN Contour-Mode MEMS Technology," *Journal of Microelectromechanical Systems*, vol. 19, pp. 570-580, 2010.

[18] S. S. Rai and B. P. Otis, "A 600µW BAW-Tuned Quadrature VCO Using Source Degenerated Coupling," *IEEE J. Solid-State Circuits*, vol. 43, pp. 300-305, 2008.

[19] H. M. Lavasani, P. Wanling, B. Harrington, R. Abdolvand, and F. Ayazi, "A 76 dB, 1.7 GHz 0.18um CMOS Tunable TIA Using Broadband Current Pre-Amplifier for High Frequency Lateral MEMS Oscillators," *IEEE J. Solid-State Circuits*, vol. 46, pp. 224-235, 2011.

[20] Y. Zhu, *et al.* , "A High Coupling Coefficient 2.3-GHz AlN Resonator for High Band LTE Filtering Application," *IEEE Electron Device Lett.*, vol. 37, no. 10, pp. 1344-1346, 2016.

[21] N. Wang, *et al.*, "Over 10% of $k^2_{eff}$ Demonstrated by 2-GHz Spurious Mode-Free Sc0.12Al0.88N Laterally Coupled Alternating Thickness Mode Resonators," *IEEE Electron Device Lett.*, vol. 40, no. 6, pp. 957-960, 2019.

[22] Y. Zhu, *et al.* , " ScAlN-Based LCAT Mode Resonators Above 2 GHz With High FOM and Reduced Fabrication Complexity," *IEEE Electron Device Lett.*, vol. 38, no. 10, pp. 1481-1484, 2017.

[23] Y. Zhu *et al.*, "An Energy Autonomous 400 MHz Active Wireless SAW Temperature Sensor Powered by Vibration Energy Harvesting," *IEEE Transactions on Circuits and Systems-I: Regular Papers*, vol. 62, no. 4, pp. 976-985, 2015.

[24] V. Mangal and P. R. Kinget, "Sub-nW Wake-Up Receivers With Gate-Biased Self-Mixers and Time-Encoded Signal Processing," *IEEE J. Solid-State Circuits*, vol. 54, No.12, pp. 3513-3524, 2019.

[25] A. Paidimarri et al., "A 2.4 GHz Multi-Channel FBAR-based Transmitter With an Integrated Pulse-Shaping Power Amplifier," *IEEE J. Solid-State Circuits*, vol. 48, No. 4, pp. 1042-1054, 2013.